Coexistence of Relaxor Behaviour and Ferromagnetic Order in Multiferroic Pb(Fe$_{0.5}$Nb$_{0.5}$)O$_3$-BiFeO$_3$ Solid Solution

SCHOLARONE™
Manuscripts

Coexistence of Relaxor Behavior and Ferromagnetic Order in Multiferroic Pb(Fe$_{0.5}$Nb$_{0.5}$)O$_3$-BiFeO$_3$ Solid Solution

Haijuan Li[1,2], Jian Zhuang[1,*], Alexei A. Bokov[2], Nan Zhang[1], Jie Zhang[1], Wei Ren[1,*], and Zuo-Guang Ye[2,*]

[1] Electronic Materials Research Laboratory, Key Laboratory of the Ministry of Education & International Center for Dielectric Research, Xi'an Jiaotong University, Xi'an 710049, China

[2] Department of Chemistry and 4D LABS, Simon Fraser University, Burnaby, British Columbia, V5A 1S6, Canada

* Corresponding Authors: zye@sfu.ca (Z.-G. Ye); jzhuang@xjtu.edu.cn (J. Zhuang); wren@xjtu.edu.cn (W. Ren)

Abstract: Coexistence of relaxor ferroelectric behaviour and ferromagnetic magnetic order in a single-phase material is of both fundamental interest and practical potential for applications. To study this rather unusual phenomenon, a series of multiferroic solid solution of (1-x)Pb(Fe$_{0.5}$Nb$_{0.5}$)O$_3$-xBiFeO$_3$ (PFN-BFO, with $0 \leq x \leq 0.6$) was synthesized in the form of ceramics using the solid-state reaction technique and its relaxor and magnetic properties were systematically characterized in this work. Structural refinements based on X-ray diffraction data at room temperature reveal the phase evolution from a monoclinic phase with Cm symmetry to pseudo-cubic phase with $Pm\overline{3}m$ symmetry with increasing BFO content. The ferroelectric phase transition and relaxor behaviour were investigated by temperature-variable dielectric spectroscopy. A temperature - composition phase diagram is constructed in terms of the T_C, T_m, Burns temperature (T_B) and freezing temperature (T_f), which delimits a ferroelectric phase (FE) for $x < 0.025$ at $T < T_C$, a non-ergotic relaxor state (NR) below T_f and an ergotic relaxor state (ER) at $T_f < T < T_B$ for $0.025 \leq x \leq 0.3$, and a paraelectric state (PE) above T_B for all the compositions. The differences in the microstructures and electric properties between this work and the literature are carefully compared and discussed, which are closely related to the preparation conditions. In addition, the

evolution of magnetic ordering with composition and temperature was investigated. A ferromagnetic order is induced by the substitution of a moderate amount of BFO ($0.1 \leq x \leq 0.2$), which exists up to room temperature. The complex magnetic phase diagram is established, which delimits an antiferromagnetic state (AFM_1) for $x = 0$, two weak ferromagnetic states, WFM_1 and WFM_2 for $0.1 \leq x \leq 0.2$, another antiferromagnetic state (AFM_2) for the compositions with $x \geq 0.25$ at $T \leq T_N$, and a paramagnetic phase (PM) for all the compositions at $T \geq T_N$. The coexistence of relaxor behaviour and ferromagnetic order at room temperature makes the PFN-BFO solid solution a particularly interesting multiferroic material.

Keywords: $Pb(Fe_{1/2}Nb_{1/2})O_3$-$BiFeO_3$ solid solution; Single-phase multiferroic; Relaxor ferroelectric; Magnetic properties; Phase diagram.

1. Introduction

Multiferroic magnetoelectrics are the materials that exhibit both magnetic and ferroelectric orders and the coupling effects between magnetization and electric polarization[1-2]. They have attracted increasing interest due to the potential advanced applications such as spintronics and high-density data storage[3-5]. In contrast to the composite multiferroics showing indirect magnetoelectric effects, the inherent magnetoelectric couplings in the single-phase multiferroic materials are fascinating from the view of fundamental physics. On the other hand, relaxor ferroelectrics form another family of important functional materials with the existence of compositional disorder and polar nanoregions, which show ultrahigh piezoelectric and electromechanical performance[6-8]. Recently, the unique magnetic relaxor is also found in single-phase multiferroic PFW single crystal[9], which indicates the existence of

relaxor behavior in magnetic systems in analogy to the ferroelectric counterpart. The combination of multiferroic and relaxor properties is expected to trigger some new magnetoelectric effects in single-phase multiferroics. Unfortunately, the materials displaying both multiferroic property and relaxor behavior are still rather scarce. In this regard, $Pb(Fe_{1/2}Nb_{1/2})O_3$ (PFN) is a promising system for the investigation of multiferroic relaxor behavior.

   PFN crystallizes in a complex perovskite structure. It is a promising multiferroic material that has attracted a great deal of attention due to its high dielectric constant, relatively large spontaneous polarization and structural complexity due to the partial B-site ordering[10-13]. Upon heating, PFN undergoes a paraelectric-ferroelectric phase transition at the Curie temperature (T_C) of 385 K[14]. Despite the numerous studies, the symmetry of the ferroelectric phase below T_C is still controversial. Some researchers suggested the ferroelectric phase to be monoclinic with the space group Cm[12,15-17], while others claimed it has the rhombohedral $R3m$ symmetry[18-20]. Besides, it was also argued that the dielectric peak of PFN corresponds to a nonrelaxor diffuse phase transition other than a normal ferroelectric phase transition, because it is a notably broadened and frequency independent[21,22]. The relaxor behavior of PFN most likely arises from the primarily disordered (and partially ordered) occupancy of Fe^{3+} and Nb^{5+} ions on the B site of the perovskite structure, which has been studied both experimentally[23-25]and theoretically[26]. Unlike most complex perovskite relaxors, PFN undergoes a magnetic ordering due to the existence of magnetic Fe^{3+} ions, leading to a G-type antiferromagnetic structure below the Neel temperature $T_N \approx 150$ K[27,28]. Beside the magnetic ordering at T_N, another low-temperature magnetic anomaly appears at 20 K, which was considered to be indicative of a magnetic glassy state below 20 K[16,28].

Moreover, short-range magnetic order was also observed above room temperature[29,30]. The coexistence of ferroelectric and magnetic ordering makes PFN a particularly interesting single-phase multiferroic material[31,32].

Many efforts have been made to elevate T_N and to enhance the magnetic property of PFN[33-35]. An efficient way to improve the dielectric and magnetic performance of PFN is to form solid solution with other perovskites, among which $BiFeO_3$ (BFO) is a promising end member. As a remarkable room temperature single-phase multiferroic material, BFO is unique as it exhibits a giant ferroelectric polarization of 50 to 100 $\mu C/cm^2$ [36], a very high ferroelectric Curie temperature $T_C \approx 1103$ K and a Neel temperature $T_N \approx 643$ K[37,38] with a G-type antiferromagnetic order below T_N and an incommensurate cycloidal spin structure[39]. The magnetic ordering and magnetoelectric coupling were first investigated in the PFN-BFO solid solution with the BFO-rich composition of 0.2PFN-0.8BFO[40,41]. Then, BFO was introduced into PFN as a minor modifier to tail the ferroic ordering temperature[33]. The solid solution of BFO-PFN shows antiferromagnetism at room temperature when the concentration of BFO is above 20%. Subsequently, the nature of the Pb-O and Fe-O bonds and the influence of the Fe-O-Fe linkages on the magnetic property were investigated in the 0.5PFN-0.5BFO composition[42]. However, several issues related to the multiferroic nature of PFN-BFO remain to be addressed. On the one hand, no ferromagnetic order has been found in the PFN-BFO solid solution at room temperature. On the other hand, the crystal symmetry and the relaxor and ferroelectric properties of PFN-BFO are still controversial in the literature. From recent studies[43-47], both the cubic and monoclinic structures were reported to occur with the substitution of BFO for PFN, and the dielectric dispersion obviously showed different types of behaviour among the different reports. One of the possible reasons for such discrepancies could be the inconsistency

in the sample quality (phase purity, ceramic density, microstructure, etc.). Therefore, the detailed phase diagrams addressing the evolution of structure symmetry, the dielectric, relaxor and magnetic properties in the PFN-BFO solid solution remain unclear, hindering the understanding of the multiferroic nature. In this work, we investigate the PFN-BFO system systematically in a wide range of compositions up to 60% BFO with small composition interval to fully explore the evolutions of structure and both magnetic and electrical properties. Based on the systematic investigations on the subtle evolution of the structure, relaxor and magnetic behaviors, the ferroelectric and magnetic phase diagrams are constructed, respectively. We also discuss the electric properties of PFN-BFO in the framework of recent literature[43-47], and found that the preparation conditions can significantly influence the microstructures and resultant relaxor behaviour. The careful preparation of the samples under optimum conditions has allowed us to reveal the coexistence of relaxor behaviour and ferromagnetic order in the PFN-BFO system at room temperature.

2. Materials Preparation and Characterization Methods

A series of the $(1-x)$PFN-xBFO solid solutions with $x = 0$, 0.025, 0.05, 0.075, 0.1, 0.125, 0.15, 0.2, 0.25, 0.3 0.35, 0.4, 0.45, 0.5, 0.55 and 0.6, were prepared in the form of ceramics by solid state reaction, using high purity ($\geq$ 99.9%) raw materials: lead oxide (PbO), iron oxide (Fe_2O_3), niobium oxide (Nb_2O_5), and bismuth oxide (Bi_2O_3). The raw oxides were weighed in stoichiometric proportions according to the intended compositions. To compensate for the evaporation of PbO and Bi_2O_3 at high temperatures, excess amounts of PbO and Bi_2O_3 (2 % mol each) were added to the starting reagents. The powders were mixed and ground by ball milling for 12 h, dried, and then pressed into pellets of 25 mm in diameter. The pellets were calcined at 800 °C for 4 h in an Al_2O_3 crucible. The calcined samples were then reground and mixed with

polyvinyl alcohol (PVA, 5 wt%) as binder, then pressed into pellets of 8 mm in diameter and about 1.7 mm in thickness. The pellets were sintered at temperatures from 950 to 1050 °C depending on compositions in a sealed Al_2O_3 crucible for 4 h to form dense ceramics. To characterize the electric properties, the ceramic samples were polished and covered with silver paste on both circular surfaces as electrodes.

The density of the sintered ceramics was measured using a standard Archimedes method. The crystal structures and phases were determined by high-resolution X-ray diffraction (XRD, PANalytical Empyrean diffractometer) with Cu-Kα_1 radiation at room temperature. The detailed structural parameters were further calculated by the Rietveld refinements using the Topas Academic software. The microstructure of the PFW-BFO ceramics was examined using the Scanning Electron Microscope (SEM, TM3030Plus) at room temperature. The dielectric properties of all the samples were measured in the frequency range from 10 Hz to 10 MHz and in the temperature range of 210 to 573 K, using a Novocontrol Concept 40 Dielectric Spectrometer. The magnetic properties were measured using a Physical Property Measurement System (PPMS, Quantum Design) and the Electron Spin Resonance System (ESR, JEOL).

3. Results and Discussion

3.1 Synthesis and structural analysis

All the $(1-x)$PFN-xBFO solid solution ceramics exhibit good quality with a high relative density of over 95% (the variations of the relative density (ρ) of the $(1-x)$PFN-xBFO solid solution ceramics with compositions are shown in Supplementary Materials Figure S1). The room-temperature XRD patterns of the $(1-x)$PFN-xBFO ceramics with different compositions are shown in Figure 1 (a) and (b), which reveal the formation of a pure perovskite phase for the compositions with $x \leq 0.4$. A trace amount of impurity phase can be found for the composition with $x = 0.45$, indicating that the solubility limit of this system is $x \approx 0.4$. The refinement of the XRD pattern by the Rietveld method

shows that the PFN ceramic crystallizes in a monoclinic with *Cm* symmetry, consistent with the literature[15-17,43-45]. With the substitution of BFO for PFN, the diffraction patterns can be well fitted with the coexistence of a monoclinic *Cm* phase and a pseudo-cubic $Pm\overline{3}m$ phase in the composition range with $0.025 \leq x \leq 0.3$, as suggested in ref. 44. Only the pseudo-cubic phase is present in the compositions with $0.3 < x \leq 0.4$. The Rietveld refinement results for the compositions with $x \leq 0.4$ are presented in Figure 1(c), and the calculated unit cell parameters for all the compositions are shown in Figure 1(d) (the detailed Rietveld refinement results for the compositions with $x \leq 0.4$ are shown in Supplementary Materials, Tables S1, S2 and S3).

As shown in Figure 1(c) and Table S2, the monoclinic *Cm* and pseudo-cubic $Pm\overline{3}m$ phases in the compositions with $x \leq 0.4$ have almost identical Bragg peak positions, but different cell parameters. This is due to the fact that the structural differences between *Cm* and $Pm\overline{3}m$ are very small; e.g., the Bragg angle (90.034°) of the *Cm* phase for $x = 0$ is very close to the Bragg angle (90°) of the $Pm\overline{3}m$ phase for $x = 0.4$. Moreover, comparing the structural data of the compositions with $x = 0$ and $x = 0.4$, we can see that the FWHM values of the (110) and (111) peaks are smaller for $x = 0.4$ than $x = 0$ (Table S2), which clearly indicates that the structure/symmetry of the PFN-BFO solid solution changes with the increase of BFO concentration. This is also consistent with the literature[44]. More sensitive diffraction techniques like synchrotron radiation would be needed to determine more accurately the phase components and to resolve the subtle structural evolution in this system.

The evolution of the *Cm* phase with composition determined in this work appears to be different from that of the samples sintered at relatively lower temperatures[43-45]. Taking the composition of $x = 0.05$ as an example, the *Cm* phase fraction increases from 56.6% for our sample to 57.3% for those samples prepared at 950 °C[44]. In fact, as the structural differences between *Cm* and $Pm\overline{3}m$ are very small, i.e., the *Cm* phase is very close to the $Pm\overline{3}m$ phase, the single $Pm\overline{3}m$ model is also used to fit the XRD patterns. As shown in Supplementary Materials Figure S2 and Table S3, the fitting results with the $R3m+Pm\overline{3}m$ model are also reasonable. For the sake of comparison, the $Cm+Pm\overline{3}m$ model is adopted in this work. Note that all the PFN-BFO samples

7

with x = 0.1, 0.2, 0.3 and 0.4 sintered at a lower temperature of 800 °C showed the monoclinic structure[43,45]. Thus, it seems that the higher sintering temperature helps stabilize the cubic symmetry while the lower sintering temperature is favorable for the formation of the *Cm* phase.
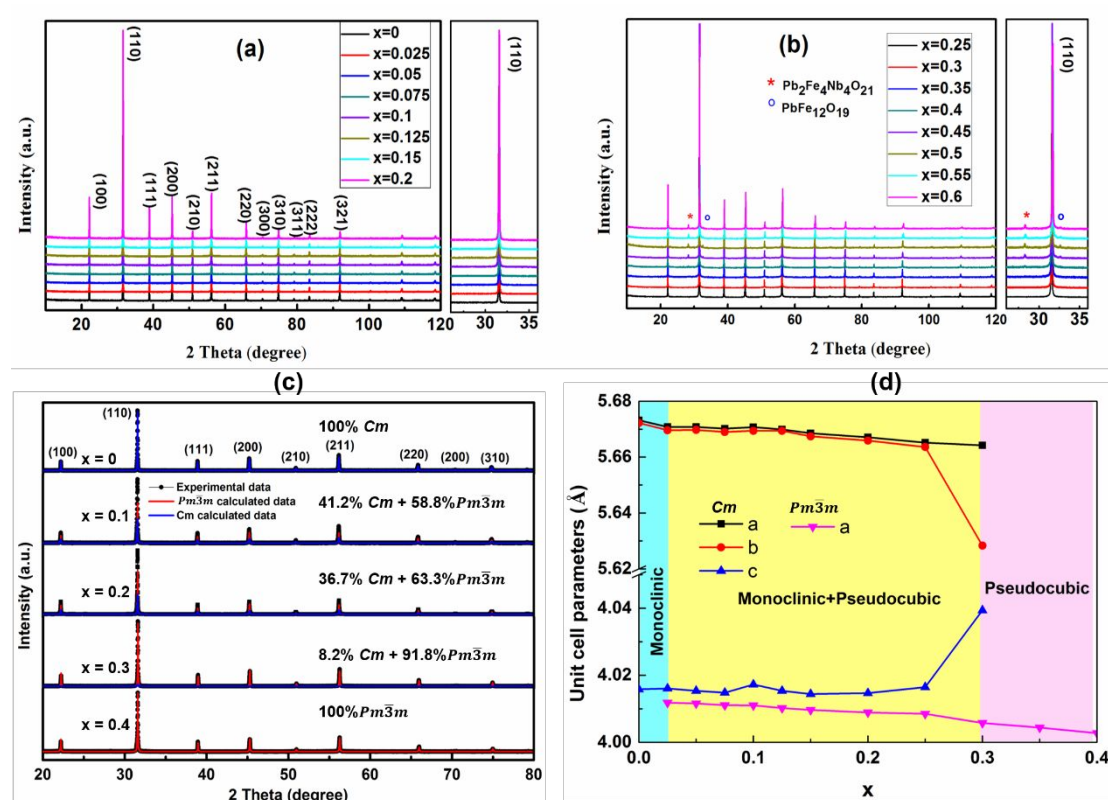

Figure 1. X-ray diffraction patterns of the as-sintered $(1-x)$PFN-xBFO ceramics with different compositions: (a) x = 0, 0.025, 0.05, 0.075, 0.1, 0.15 and 0.2, and (b) x = 0.25, 0.3, 0.35, 0.4, 0.45, 0.5, 0.55 and 0.6, at room temperature. (c) Rietveld refinement results using the monoclinic *Cm* and pseudo-cubic $Pm\overline{3}m$ symmetries for the compositions with x = 0, 0.1, 0.2, 0.3, and 0.4, respectively, with the Bragg peak positions indicated for the *Cm* (blue, top) and $Pm\overline{3}m$ (red, bottom) phases, and the various mixtures of Cm + $Pm\overline{3}m$ phases (middle). (d) Variations of the unit cell parameters of the $(1-x)$PFN-xBFO solid solution with compositions.

The microstructure of the as-sintered $(1-x)$PFN-xBFO ceramics is imaged by SEM technology. The results of selected compositions are shown in Figure 2. The average grain size of the PFN ceramic is about 8 μm. The ceramics of compositions with $x \leq$ 0.075 exhibit well-developed irregular grains with large size, similar to the PFN ceramic. With further increase of BFO content up to x = 0.4, the average grain size decreases, with the average grain size being reduced to about 2 μm for x = 0.4. The

formation of smaller grains is due to the reduced sintering temperature. However, an

obvious increase in grain size is observed for the composition with $x > 0.5$. It is due

to the lower sintering temperature of BFO[48,49] than PFN[12,50], the BFO-rich

compositions are more likely to form a liquid phase during sintering

through eutectic reaction, which is beneficial to the grain growth[51]. Note

that the samples studied in this work exhibit larger grains than the reported in refs. 43

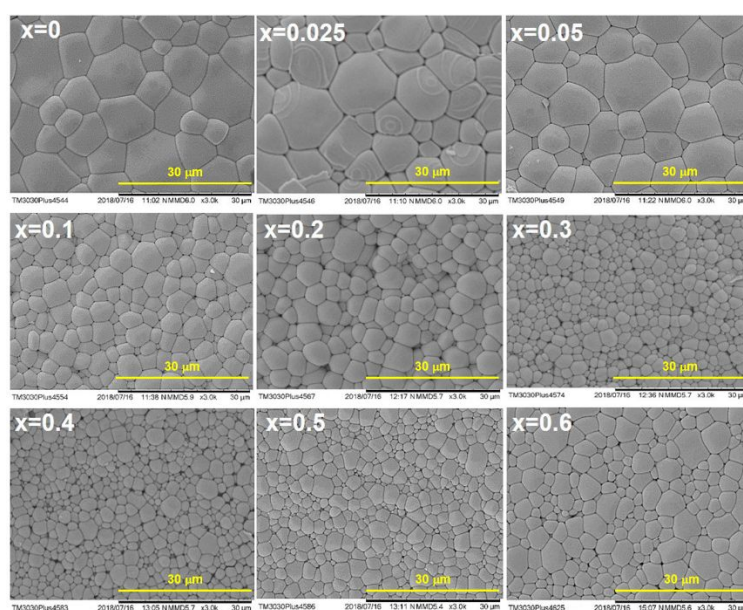and 44, which is believed to be related to the higher sintering temperature used here.

Figure 2. Room temperature SEM images of the as-sintered (1-x)PFN-xBFO ceramics of selected compositions.

3.2 Dielectric properties

Figure 3 shows the temperature dependences of the real part of dielectric permittivity (ε') and loss tangent ($tan\delta$) for the (1-x)PFN-xBFO ceramics (x = 0, 0.05, 0.1, 0.15, 0.2 and 0.3) measured at the frequencies from 10 Hz to 10 MHz (the dielectric results for the other compositions studied can be found in Supplementary Materials

Figure S3). For pure PFN a sharp dielectric peak is observed at T_C = 369 K, which is independent of frequency, signifying the ferroelectric to paraelectric phase transition Curie temperature. This is consistent well with the literature[21,22,44]. At high temperatures (> T_C), significant frequency dispersion appears, which could be attributed an extrinsic Maxwell-Wagner relaxation[52-58]. The substitution of BFO for PFN has a remarkable effect on the dielectric behavior of the PFN-BFO ceramics. For the compositions with $0.025 \leq x \leq 0.3$ the temperature of dielectric maximum (T_m) shifts to higher temperatures with increasing frequency, indicating a typical relaxor behavior. However, with the increase of BFO concentration ($x \geq 0.15$), the values of T_m at the low frequencies gradually become undistinguishable. Waser et al.[59] reported that the oxygen vacancies and related defects play an important role in the low frequency relaxation in oxide ferroelectric materials. The use of saturated oxygen atmosphere during the sintering can prevent (or minimizes) the reduction of Fe^{3+} to Fe^{2+} and reduce the amount of oxygen vacancies, as reported in ref. 44, which consequently results in a lower electrical conductivity and dielectric losses of the material, so that the clear relaxation behaviour can be observed in the compositions with x up to 0.2. Also, the relatively high sintering temperatures can lead to the formation of high-quality and dense ceramics with well-developed grains and less pores, which can also be beneficial to the dielectric properties. In comparison, the ceramic samples prepared at low temperature in air were more conductive, and moreover, the dielectric peak looked like frequency independent[43]. As a result, the characteristic relaxation behaviour smeared out and became invisible. Especially in the compositions with a high BFO concentration, the dielectric leakage due to the increase in oxygen vacancies and the formation of mixed valence states of Fe^{2+}/Fe^{3+} made the relaxor-type dielectric maxima undistinguishable for the compositions with $x > 0.30$. It can be seen the good quality ceramic samples with reduced dielectric loss are critical for the study of the detailed evolution of relaxor behaviors studied in this work.
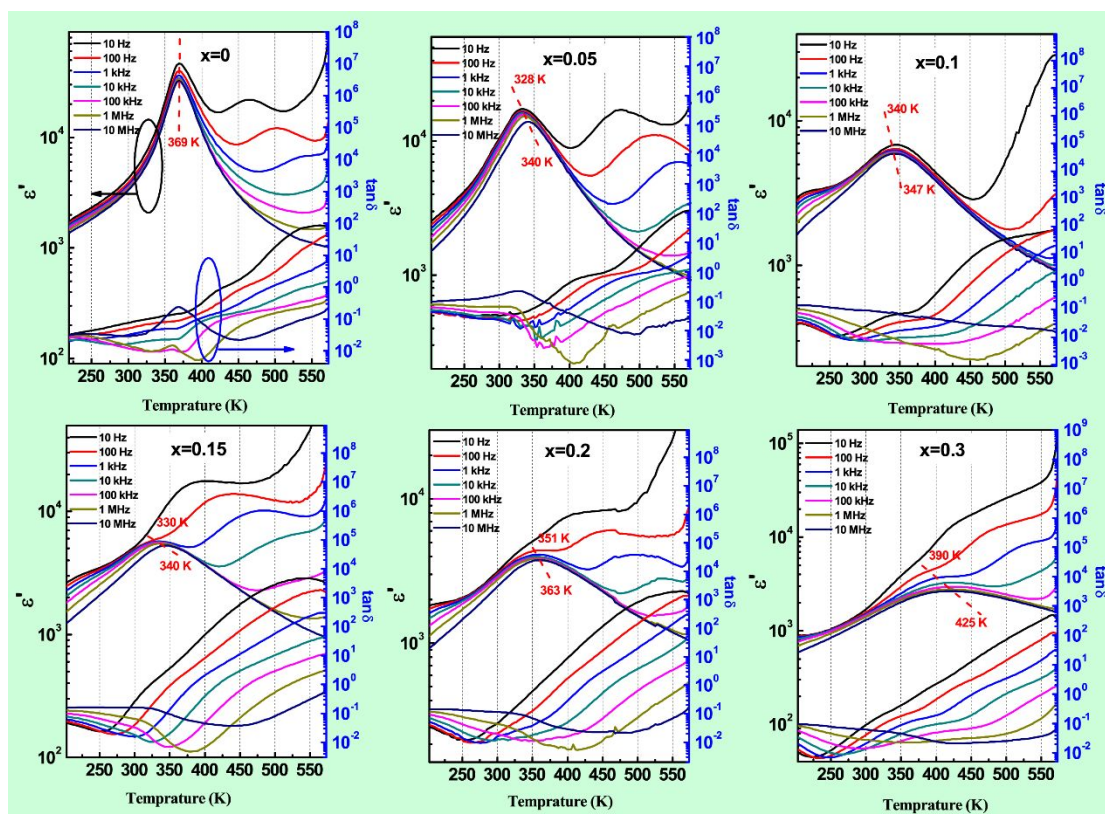
Figure 3. Temperature dependences of the real part of dielectric permittivity (ε') and loss tangent ($tan\delta$) for the (1-x)PFN-xBFO (x = 0, 0.05, 0.1, 0.15, 0.2 and 0.3) ceramics measured at frequencies from 10 Hz to 10 MHz.

To study the evolution of relaxor behavior of the (1-x)PFN-xBFO ceramics, the values of T_m at 1 kHz and the difference in T_m (ΔT_m) are plotted as a function of compositions, as shown in Figure 4. The difference in the T_m values measured at two different frequencies, typically $\Delta T_m = T_m$ (10 MHz) - T_m (1 kHz), can be used to characterize the degree of relaxor [60,61]. T_m shows a complex behavior with increasing x. First, T_m decreases from 369 K for pure PFN to 332 K for 0.925PFN-0.075BFO. This is different from the PFN-BFO samples sintered at a lower temperature of 950 °C[44], which had the lowest value of T_m for the composition with x = 0.2. Subsequently, it reaches sort of saturation around 345 K for the composition with x = 0.125. Finally, a monotonous increase in T_m is revealed with further increase of x. In addition, with increasing BFO content, ΔT_m shows an increasing trend on the whole, indicating an

enhanced relaxor character with the substitution of BFO for PFN. This is consistent

well with the literature[44]. Similar to other relaxor ferroelectrics with complex perovskite

structure, the enhanced relaxor behavior in PFN-BFO is believed to be closely related

to the increased chemical disorder and enhanced random electric field arising from the

coupled aliovalent substitutions the cations on both the A and B sites[62,63]. We also can

see that the ε_m' at T_m first significantly decreases from 36,300 for $x = 0$ to 2,700 for $x =$

0.125, and then increases with further increase of BFO ($x \geq 0.15$). At the same time, the

dielectric peak becomes increasingly diffuse and broad with increasing x (the

temperature dependences of the dielectric permittivity (ε') the variations of permitivity

maximum ε_m' with compositions $x \leq 0.3$ at 1 kHz are shown in Figure S4(a) and (b) in

the Supplementary Materials). The increase of ε_m' for compositions with $x = 0.15$ is

related to the high temperature Maxwell-Wagner relaxation approaching T_m with
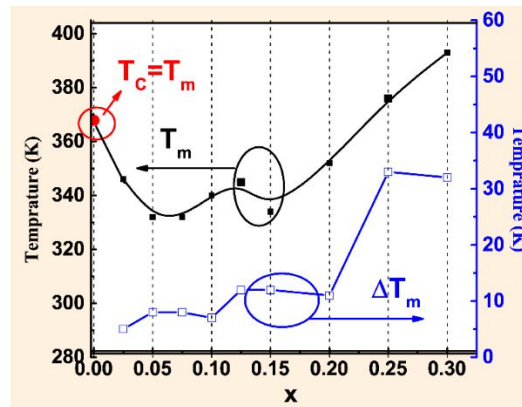
increasing concentration of BFO.

Figure 4. Variations of the dielectric peak temperature T_m at 1 kHz and ΔT_m (K) [$\Delta T_m = T_m$ (10 MHz) -
T_m (1 kHz)] as a function of composition for the (1-x)PFN-xBFO ceramics.

A remarkable feature which has been observed[64] in relaxor ferroelectrics is the

satisfaction to the Vogel-Fulcher (VF) law for T_m and the corresponding frequency:

$$f = f_0 \exp\left(-\frac{E_a}{k_B(T_m - T_f)}\right) \quad , \tag{1}$$

where f is the measurement frequency, f_0 and E_a are the fitting parameters, T_f stands for the freezing temperature, and k_B is the Boltzmann constant. The VF fitting results for the $(1-x)$PFN-xBFO ceramics with the composition $x = 0.05$ is presented in Figure 5(a) as an example. The fitting is satisfactory, confirming the relaxor nature for the $(1-x)$PFN-xBFO ceramics with compositions $0.025 \leq x \leq 0.3$. In comparison, in the results reported in ref. 44, the VF fitting was only satisfactory for the compositions with $x = 0.05$, 0.10 and 0.20. The fitting parameters to the VF law are shown in Table 1. Note that the influence from the above-mentioned extrinsic leakage and Maxwell-Wagner relaxation cause that the VF fitting cannot be performed for those compositions with $x > 0.3$. The variations of the fitting parameter T_f with composition for the series of compounds are shown in Figure 5 (c).

It is worth further discussing the differences between some of our results and those reported in refs. 43, 44 and 45. For the same compositions, the different degrees of relaxor observed could be related to the different degrees of compositional disorder, which is known to affect the relaxor behaviour. And the compositional disorder could be related to the sintering temperatures. The higher sintering temperature can result in a lower degree of compositional disorder, which then gives rise to weaker relaxor behaviour. Therefore, it is possible to tune the relaxor behaviour in the PFN-BFO system by modifying the preparation conditions.

Table 1. Parameters of fitting to the Vogel-Fulcher law for the $(1-x)$PFN-xBFO ceramics

x	0.025	0.05	0.075	0.1	0.125	0.15	0.2	0.25	0.3
T_f/K	318	299	295	306	313	312	323	334	338
E_a/eV	0.072	0.049	0.080	0.100	0.072	0.016	0.038	0.034	0.057
f_0/Hz	7.1×10^{13}	5.7×10^{8}	4.3×10^{11}	1.2×10^{15}	1.2×10^{11}	9.8×10^{5}	4.1×10^{7}	6.7×10^{5}	8.9×10^{5}

It is known that for normal ferroelectrics the Curie-Weiss (CW) law is satisfied at $T > T_m$:

$$\varepsilon' = \varepsilon_\infty + C/(T - T_{cw}), \qquad\qquad (2)$$

where T_{CW} is the Curie-Weiss temperature, C is the Curie constant, and ε_∞ is the parameter representing the possible temperature-independent (non-ferroelectric) contribution to the permittivity (including the contribution of high-energy phonon modes and electronic polarization). In relaxors, however, the CW law is found to be satisfied at $T > T_B$ (Burns temperature), which is generally much higher than T_m[65]. In the PFN-BFO system, the additional non-ferroelectric polarization mechanism dominates the dielectric permittivity at low frequencies for the high temperature parts of the ε' - T curve (see above). Therefore, the dielectric data measured at high enough frequency (e.g. 1 MHz) at which this parasitic contribution becomes negligible are selected to fit the CW law. It is found the CW law is well satisfied for all compositions with $0.025 \leq x \leq 0.3$, suggesting the paraelectric (PE) nature above T_B. The result for the composition with $x = 0.05$ is shown in Figure 5 (b) as an example. The variations of the fitting parameters T_{CW} and T_B with composition for the series of compounds are shown in Figure 5 (c).
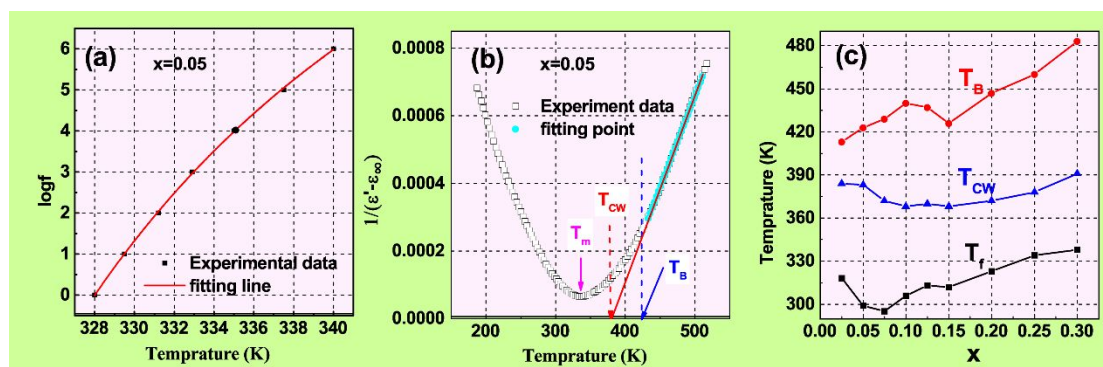
Figure 5. (a) Relationship between the temperature of maximum permittivity (T_m) and frequency as fitted to the VF law (Eq. (1)). (b) Temperature dependence of the dielectric constant at 1 MHz and the fitting curve to the CW law (Eq. (2)), for the (1-x)PFW-xBFO ceramic with composition x = 0.05 (Filled square symbols: experimental data; Read line: fitting line; Green solid symbols: fitting points). (c) Variations of the characteristic temperatures as a function of composition for the (1-x)PFW-xBFO ceramics with compositions $x \leq 0.3$ (T_f stands for the freezing temperature from the VF analysis, T_B and T_{CW} stand for the Burns temperature and the Curie-Weiss temperature from CW fitting results, respectively).

3.3 Magnetic properties

The magnetization (M) of the (1-x)PFN-xBFO ceramics was measured as a function of temperature (T) to investigate the magnetic phase transitions. Figure 6 shows the results for selected compositions (x = 0.05, 0.1 and 0.15) measured upon cooling from 300 K to 5 K under an applied field of 500 Oe (the M(T) curves of the other compositions can be found in Supplementary Materials Figure S5). No meaningful anomaly can be found on the M(T) curve of PFN in the temperature range investigated, which is consistent with the result reported on PFN single crystal by Stock *et. Al*[29]. Note a weak anomaly around the Neel temperature T_N = 155-160 K was reported on ceramic sample when the applied magnetic field was relative large[27]. Interestingly, with the substitution of a small amount of BFO (x = 0.025), an observable anomaly appears at 155 K, as shown in Figure S5, which indicates a transition of the magnetically ordered state induced by the substitution of BFO. As the concentration of

BFO increases from $x = 0.025$ to $x = 0.2$, this magnetic transition temperature increases from 155 K to 290 K, indicating an enhancement of the magnetic order. In order to describe the complex magnetic transition behavior, the transition temperatures are marked as T_N for the compositions with $x \leq 0.075$ and T_C for the compositions with $0.1 \leq x \leq 0.2$ (with ferromagnetic ordering; see below), respectively. The variations of T_N and T_C as a function of composition are shown in Figure 6 (d). As the concentration of BFO is greater than $x = 0.2$, the transition temperature moves above room temperature (out of measurement range). The increase of the Neel temperature and the associated enhancement of magnetic order with the increasing concentration of BFO, can be attributed to the increased concentration of magnetic Fe^{3+}, which strengthens the superexchange couplings of Fe^{3+}-O-Fe^{3+}. The magnetization at a selected temperature below T_N (50 K) is also plotted as a function of composition in Figure 6(d). It can be seen that the change in magnetization is negligible with x increasing from 0 to 0.075. Subsequently, a sharp increase in magnetization occurs at $x = 0.1$ with a maximum value of ~ 0.025 emu/g. With further increase of BFO concentration, the magnetization decreases to 0.004 emu/g for $x = 0.3$. Such a complex behavior of magnetization is related to the complex magnetic orderings in the solid solution system, which will be discussed later on.
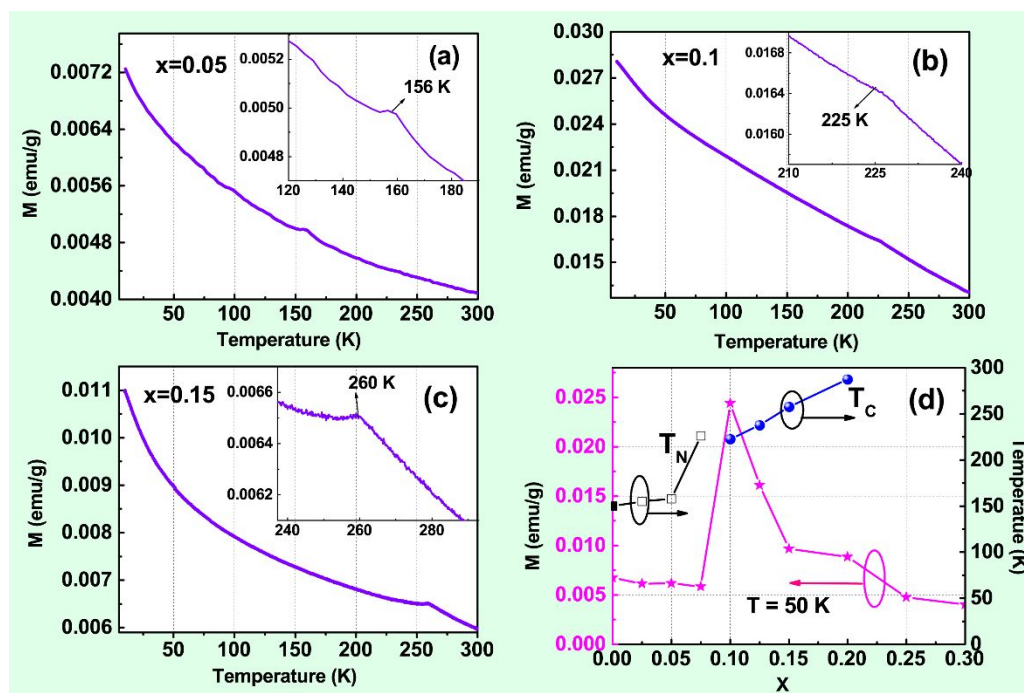
Figure 6. Variation of the magnetization (FC curves) for the (1-x)PFN-xBFO ceramics for selected compositions: (a) x = 0.05, (b) x = 0.1, and (c) x = 0.15. The insets are the enlarged views. (d) Variations of T_N, T_C and the magnetization measured at 50 K as a function of composition, the value of T_N for PFN was taken from Ref. 18.

The magnetic hysteresis (M-H) loops of the (1-x)PFN-xBFO solid solutions are measured at 100 K, 200 K and 300 K under an applied field of 15 kOe for all the compositions. Figure 7 shows the results for selected compositions with x = 0.0, 0.05, 0.1, 0.125, 0.15, and 0.2 (the M-H loops of the other compositions are shown in Supplementary Materials Figure S6). The compositions with $x \leq 0.075$ show an almost linear M-H relation at the temperatures of 100, 200 and 300 K, i. e. both above and below T_N, indicating the magnetic anomaly at T_N mainly corresponds to a paramagnetic to antiferromagnetic phase transition (upon cooling). For the compositions with $0.1 \leq x \leq 0.2$, an appreciable hysteresis loop with a non-zero remnant magnetization appears at all the three temperatures, suggesting the existence of a (weakly) ferromagnetic state at temperatures above and below T_C. In other words, the magnetic anomaly at T_C for the

compositions with $0.1 \leq x \leq 0.2$ in Figure 6(d) is associated with the phase transition from one (weakly) ferromagnetic state (WFM$_1$) to another (weakly) ferromagnetic state (WFM$_2$), which is different from the paramagnetic to antiferromagnetic transition in PFN and PFN-BFO with $x \leq 0.075$. It is particularly interesting to note that the induced ferromagnetic state exists at room temperature for the compositions with $0.1 \leq x \leq 0.2$. This implies that the substitution of BFO for PFN results in a room-temperature ferromagnetic order in the PFN-BFO solid solution and the ferromagnetic to paramagnetic phase transition should take place above 300 K. With further increase of BFO content, the hysteresis loops of the samples gradually disappear and only linear M-H relations can be observed at all the measurement temperatures, indicating a mainly antiferromagnetic state for the compositions of $x \geq 0.25$.
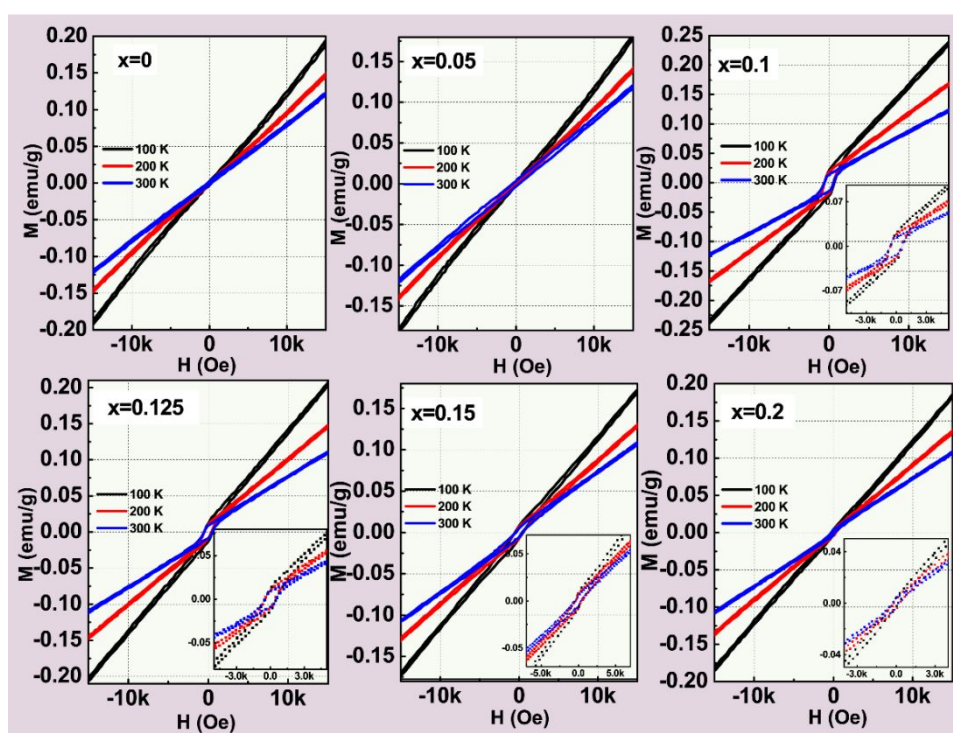

Figure 7. Magnetization (M) vs applied magnetic field (H) hysteresis loops of the (1-x)PFN-xBFO solid solution with selected compositions (x = 0.0, 0.05, 0.1, 0.125, 0.15, and 0.2), measured at 100 K, 200 K and 300 K. The insets are the enlarged views of the M-H loops.

The linear fittings of the M-H curves at high magnetic fields (H ≥ 9 kOe) are performed for all the compositions. Figure 8(a) shows the fitting results for PFN as an example. The linear fitting parameters, namely, the slope and intercept, represent the magnetic susceptibility (χ_e) and saturated magnetization (M_s), respectively. The variations of the calculated M_s and χ_e with composition are plotted in Figure 8 (b) and (c). When $x \leq 0.75$, M_s generally shows a very small value close to zero, which increases slightly upon cooling. The M_s value increases sharply and reaches the maximum at $x =$ 0.1. The maximum values of the saturated magnetization at 100 K, 200 K and 300 K are found to be 0.023 emu/g, 0.02 emu/g and 0.017 emu/g, respectively. Further increase of BFO concentration leads to a decrease in the M_s value, which drops to nearly zero for the compositions with $x > 0.25$. As shown in Figure 8(c), χ_e exhibits a similar trend with increasing BFO content, and the maximum value of χ_e is also located at $x =$ 0.1. Upon cooling, it increases from 8.8×10^{-6} emu/(g•Oe) at 300 K to 1.4×10^{-5} emu/(g•Oe) at 100 K. Interestingly, the trends of M_s and χ_e with compositions are consistent with the corresponding trend of the magnetization measured at small magnetic fields shown in Figure 6(d), strongly indicating the strongest ferromagnetism for the composition with $x = 0.10$.
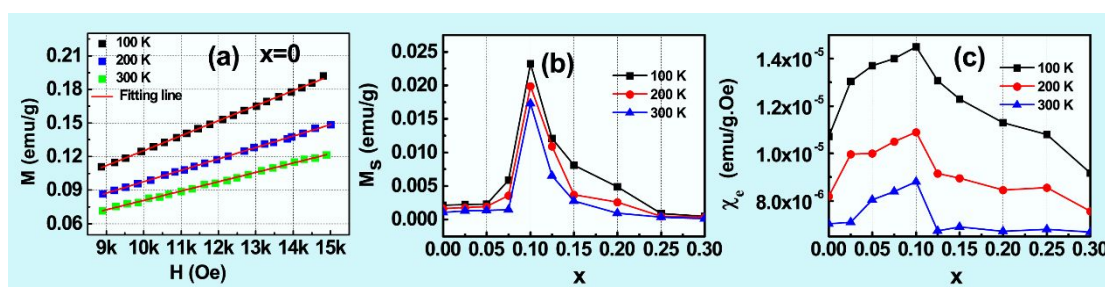

Figure 8. (a) Dependence of the magnetization (M) on magnetic field (H) and the linear fitting curves for PFN at different temperatures. (b) and (c) Variations of the saturated magnetization (M_s) and magnetic susceptibility (χ_e) of the (1-x)PFN-xBFO solid solution with composition measured at different temperatures.

To further study the complex magnetic orderings of the PFN-BFO solid solution, electron spin resonance (ESR) spectroscopic measurements were performed to probe the spin states of the magnetic ions. Figure 9 (a), (b) and (c) show the ESR spectra of the PFN-BFO ceramics measured at room temperature. A weak resonance peaks are observed at 3210 Oe for the compositions with $x \leq 0.075$. More pronounced resonance peaks appear at $3600 \sim 3800$ Oe for the compositions with $0.1 \leq x \leq 0.2$, which confirms the formation of ferromagnetic component. The resonance peaks are almost attenuated for $x > 0.2$, which is consistent with the antiferromagnetic nature. The magnetic g-factor is calculated for different compositions by the following equation:

$$g = h\nu/\beta H, \tag{3}$$

where h is Planck's constant, β is the Bohr magneton, ν is the resonance frequency of the sample cavity, and H is the central magnetic field of the resonance absorption signal. The calculated g-factor for the compositions with $x \leq 0.075$ is very close to the value of 2, confirming the paramagnetic nature at room temperature. For compositions with $0.1 \leq x \leq 0.2$, the calculated values of g-factor are in the range of $1.73 \sim 1.83$, which deviate significantly from 2, indicating the formation of a magnetic order. This supports the weakly ferromagnetic character observed from the M-H loops with non-zero remnant magnetization. Two important ESR parameters, the peak-to-peak line width (ΔH_{PP}) and the peak intensity (H_{pp}) reflecting the total number of unpaired electrons in the sample related to the relaxation characteristic of the system, ΔH_{PP} and H_{pp} are also plotted as a function of composition in Figure 9(d). Both the ΔH_{PP} and H_{pp} values show a maximum in the composition range of $0.1 \leq x \leq 0.2$ where the ferromagnetic state sets in. Outside of this range, ΔH_{PP} and H_{pp} decrease significantly, confirming the absence of such a ferromagnetic order.
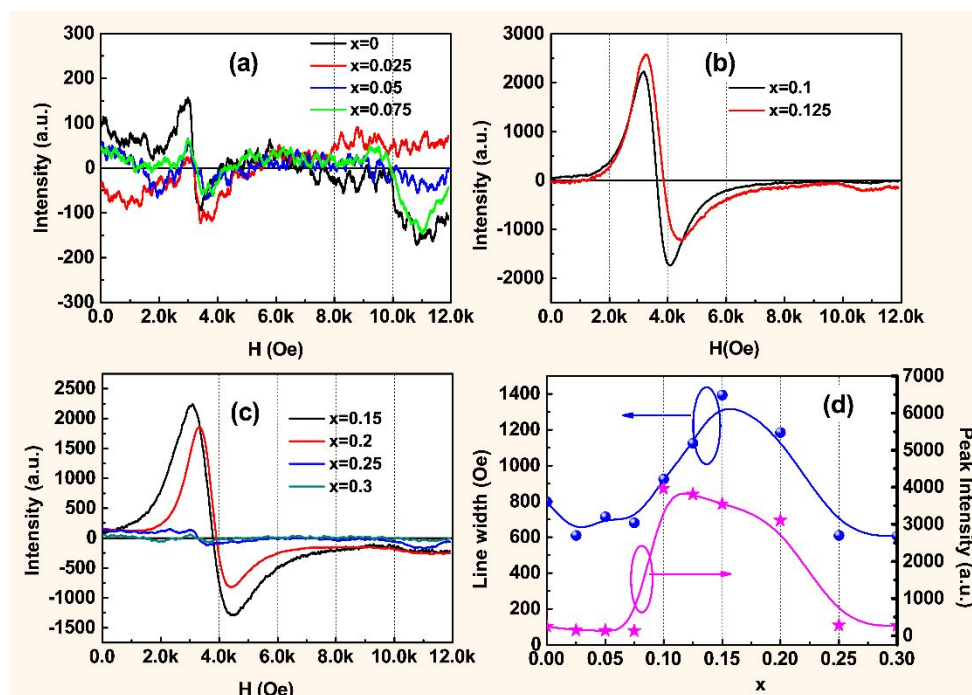
Figure 9. Room temperature ESR spectra for the different compositions of the (1-x)PFN-xBFO system: (a) x = 0, 0.025, 0.05, 0.075, (b) x = 0.1 and 0.125, and (c) x = 0.15, 0.2, 0.25 and 0.3. (d) Variations of the peak-to-peak line width and peak intensity with composition.

As one of the most important criteria for multiferroics, the appearance of ferromagnetic order in the composition range of $0.1 \leq x \leq 0.2$ is meaningful and needs to be discussed further. As shown in Figure 8(b), the saturated magnetization (M_s) at room temperature decreases with increasing BFO content from 0.0173 emu/g for x = 0.1 to 0.0009 emu/g for x = 0.2, indicating the weakening of the ferromagnetic order. Simultaneously, the symmetry parameter (P_{asy}), which is defined as

$$P_{asy} = (1 - h_U/h_L), \qquad (4)$$

where h_U is the height of the absorption peak above the base line and h_L is the height of the absorption peak below the base line of the first derivative of the magnetic resonance absorption signal, can be used to indicate the extent of the anisotropy in the magnetic structure of the samples. It is found that the calculated value of P_{asy} decreases substantially with increasing x, from -0.28 for x = 0.1 to -1.27 for x = 0.2, indicating an

increasing anisotropy of magnetocrystalline structure, which could be origin of the induced ferromagnetic properties observed in this solid solution system[66].

3.4 Dielectric and magnetic phase diagrams

The above-mentioned studies of the relaxor behavior and magnetic properties allow us to establish both the dielectric and magnetic phase diagrams for the PFN-BFO solid solution system. First, based on the analyses of the structural phase transition and relaxor behavior, the dielectric phase diagram of the PFN-BFO system is constructed in terms of the ferroelectric T_C, Burns temperature T_B and freezing temperature T_f, as shown in Figure 10 (a). The compositions on the PFN-rich side ($x < 0.025$) possess the ferroelectric (FE) phase at room temperature, which transforms into the paraelectric (PE) phase at T_C. With increasing BFO content, the FE phase gradually develops into a typical relaxor ferroelectric (RFE) state for compositions of $x \geq 0.025$, and the boundary for this FE to RFE crossover is located near $x = 0.025$, as marked by the vertical black dash line. For the compositions with $x > 0.025$，the phase diagram delimits three zones separated by T_B and T_f. The low temperature zone defines the nonergodic relaxor (NR) state existing below T_f, where the polar nanoregions (PNRs) become frozen and the number and size of PNRs remain practically the same at any temperature. The intermediate temperature zone at $T_f < T < T_B$ indicates the ergodic relaxor (ER) state, where the number and size of PNRs decrease with increasing temperature. The high temperature zone describes the PE phase appearing at $T > T_B$, where the PNRs disappear. Thus, this phase diagram represents the characteristics of the dipole dynamics in the PFN-BFO solid solution, which is reminiscent of a typical relaxor[65].

On the other hand, based on the measurements and analysis of magnetic properties, a magnetic phase diagram is proposed for the PFN-BFO solid solution, as shown in Figure 10 (b). It reveals a rather complex scenario for the evolution of magnetic ordering. The compositions with $x < 0.1$ exhibit an antiferromagnetic (AFM$_1$) phase at low temperatures, which originates from the antiferromagnetic phase in PFN. Upon heating, the AFM$_1$ phase transforms into a paramagnetic (PM) phase at T_N, which gradually increases with increasing BFO content due to the enhanced antiferromagnetic coupling. With increasing content of BFO, the compositions with $0.1 \leq x \leq 0.2$ exhibit a weakly ferromagnetic (WFM$_1$) state below T_C, and another weakly ferromagnetic (WFM$_2$) state above T_C. The WFM$_2$ state exists at room temperature, and should transform into the paramagnetic phase at a higher temperature (yet to be determined; the green dash line is just a schematic representation). With higher concentration of BFO, the composition with $x \geqslant 0.25$ reveals an antiferromagnetic state (AFM$_2$) in the temperature range between 5 and 300 K, which is expected to transform into the PM phase above room temperature (the green dash line is just an estimated AFM$_2$ - PM phase boundary, extrapolated from $T_N = 643$ K for BFO[37,38]). Of particular interests is the intermediate region with $0.1 \leq x \leq 0.2$ where ferromagnetic phases are induced by the BFO substitution, one of which exists up to room temperature. The ground state of the Fe^{3+} ion arrangement in pure PFN leads to an antiferromagnetic order. The substitution of BFO for PFN causes the AFM Neel temperature to increase for $x < 0.1$, but also unbalance the AFM ground state, leads to the ferromagnetic (or ferrimagnetic) ordering in the compositions with $0.1 \leq x \leq 0.2$, and the formation of the WFM states.

With higher substitution rate, the increased chemical disorder could disrupt the WFM

ordering and restore the AFM state for the compositions with $x > 0.2$.

The possible reasons for the evolution of magnetic phases and formation of WFM

states found in the PFN-BFO solid solution may be related to the compositional and

structural changes induced by the substitution of BFO for PFN. It is known that the G-

type AFE ordering in oxide perovskites like PFN and BFO arises from the

superexchange interaction of the Fe^{3+}-O-Fe^{3+} type and depends mainly on two factors,

i.e. the concentration of the magnetic ions (Fe^{3+}) and the distance (and angle) of the

interaction. Based on the results of the BFO-$PbTiO_3$ system[67], the magnetic ordering

temperature is related to the concentration of the magnetic ions: the higher the

concentration of the magnetic ion, the higher magnetic ordering temperature. This can

explain the fact that the T_N (or T_C) of the PFN-BFO solid solution increases with the

increase of BFO concentration which introduces a relatively higher amount Fe^{3+} on the

B-site, as shown in Fig. 6(d) and Fig. 10(b). In addition, the "critical coupling distance"

of the cooperative magnetic interaction for the magnetic ordering is different for the

phases of different structures, since the magnetic moments and angles of the two

neighbouring Fe^{3+} ions in the different structures are different. In the pseudo-cubic

phase, the atomic distance of Fe^{3+}-O-Fe^{3+} is equal to the lattice parameter a and the

angle of Fe^{3+}-O-Fe^{3+} linkage is almost 180°, while the atomic distance of Fe^{3+}-O-Fe^{3+}

in the monoclinic phase is larger than the lattice parameter c and the angle of Fe^{3+}-O-

Fe^{3+} linkage is less than 180°. With the substitution of a small amount of BFO ($x \leq$

0.075), the monoclinic phase is still dominant (according to the XRD data), the nature

of the antiferromagnetic interaction of PFN is basically preserved. With further increase

of BFO concentration ($0.1 \leq x \leq 0.2$), the induced structural change with a larger ratio

of pseudo-cubic to monoclinic phases (> 50%) and the increased Fe^{3+}-O-Fe^{3+}

interaction pathways due to a higher concentration of Fe^{3+} are expected to result in some kind of canting of the antiferromagnetic ordering, leading to the appearance of weak ferromagnetism. At higher concentrations of BFO ($x \geq 0.25$), it is possible that the spiral spin modulation, as known in BFO[39], starts to take effect, which could then destroy the WFM order and restore the AFM state.
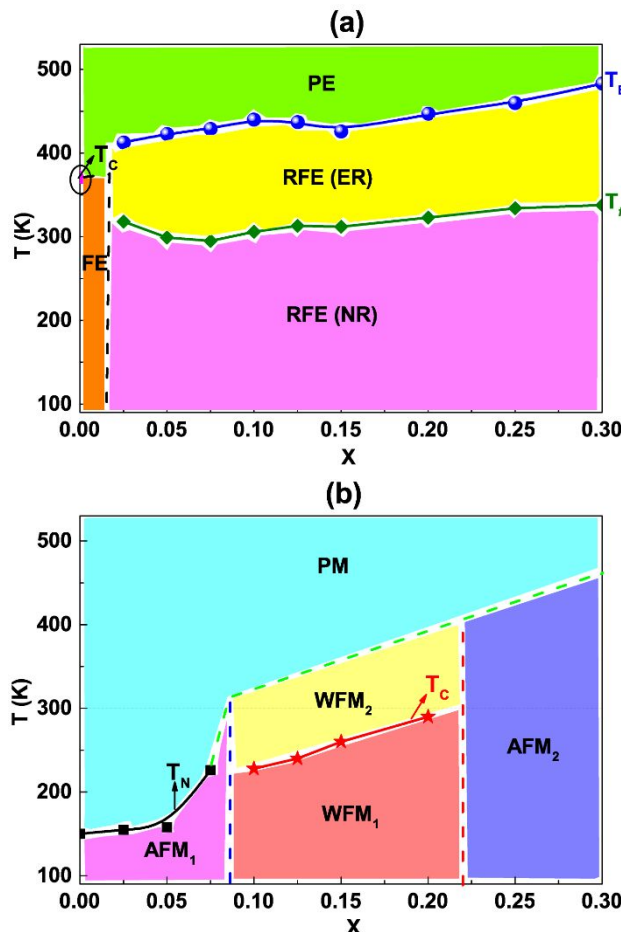

Figure 10. (a) The dielectric phase diagram of the (1-x)PFN-xBFO ($x \leqslant 0.3$) system, which delimits the ferroelectric phase (FE), the paraelectric phase (PE), the relaxor ferroelectric (RFE) states with ergotic relaxor (ER) and nonergotic relaxor (NR). The characteristic temperatures are shown: T_C is the ferroelectric phase transition temperature, T_B stands for the Burns temperature from Curie-Weiss law, and T_f is the freezing temperature from Vogel-Fulcher analysis. (b) The magnetic phase diagram of the (1-x)PFN-xBFO ($x \leqslant 0.3$) system, which delimits the antiferromagnetic phase below T_N for $x < 0.1$, the weakly ferromagnetic phases (WFM$_1$ and WFM$_2$) for $0.1 \leqslant x \leqslant 0.2$, the antiferromagnetic phase

AFM$_2$ for $x > 0.20$, and the paramagnetic phase (PM) at high temperatures. The green dash line is an estimated phase boundary extrapolated from the $T_N = 643$ K for BFO[37,38].

4. Conclusions

To investigate the coexistence of relaxor behavior and magnetic properties, the multiferroic solid solution of $(1-x)$Pb(Fe$_{0.5}$Nb$_{0.5}$)O$_3$-xBiFeO$_3$ (PFN-BFO)   (with $0 \leq x \leq 0.6$) was synthesized by the solid-state reaction technique. Structural refinement using X-ray diffraction data reveals that the formation of a monoclinic phase with Cm symmetry with $x = 0$, the coexistence of monoclinic phase and pseudo-cubic phase $Pm\bar{3}m$ symmetry for the compositions with $0.025 \leq x \leq 0.3$, while the appearances of only the pseudo-cubic phase for the compositions with $0.3 < x \leq 0.4$. The solubility limit of the solid solute system is found to be $x = 0.4$. The pure PFN shows a ferroelectric to paraelectric phase transition at $T_C = 369$ K. The substitution of BFO leads to crossover from ferroelectric state to relaxor behavior which develops gradually with increasing BFO concentration. It is interesting to find that both the microstructure and the relaxation behaviors can be tuned by the preparation conditions, which probably can affect the composition disorder of as-sintered ceramics. Based on the analyses of dielectric properties and relaxor behavior, a partial phase diagram of the $(1-x)$PFN-xBFO solid solution system has been established for the composition range of $0 \leq x \leq 0.3$, which delimits the ferroelectric (FE), the paraelectric (PE), ergotic relaxor (ER) and nonergotic relaxor (NR) states.

The magnetic properties of $(1-x)$PFN-xBFO multiferroic solid solutions ($x \leq 0.3$) have been investigated and discussed. In addition to the antiferromagnetic state below T_N on the PFN-rich side, ferromagnetic orders are induced in the solid solution with 0.1

26

$\leq x \leq 0.2$, with one which existing at room temperature. Based on the magnetic characterizations, a magnetic phase diagram has been established, which reveals a complex picture of the various magnetic phases, from the antiferromagnetic (AFM_1) order for $x < 0.1$ to the weakly ferromagnetic phase (WFM_1 and WFM_2) for $0.1 \leq x \leq 0.2$, and then to the antiferromagnetic (AFM_2) for compositions with $x \geq 0.25$, together with the paramagnetic (PM) phase at high temperatures. The evolution of magnetic ordering could be attributed to the composition and structural changes for PFN-BFO ceramics with the increase of BFO substitution.

The combined dielectric and magnetic phase diagrams show that the relaxor ferroelectric state and the ferromagnetic phase coexist in the PFN-BFO solid solution with $0.1 \leq x \leq 0.2$ at room temperature. This is the most interesting feature of this multiferroic system. Considering that the coupling between short range ferroelectric and magnetic order demonstrated in PFN at low temperatures[29], the successfully induced weak ferromagnetic order with magnetic clusters and the tunable relaxor state with differently correlated polar clusters, make the PFN-BFO solid solution a viable multiferroic material in which enhanced magnetoelectric coupling is expected, providing more degrees of freedom for the design of magnetoelectric memory and spintronic devices. Such magnetoelectric coupling may take place via multiferroic (electric and magnetic) clusters which can be switched by the action of an electric field and a magnetic field, respectively, as in the case of $0.4BiFe_{0.9}Co_{0.1}O_3$-$0.6Bi_{1/2}K_{1/2}TiO_3$ relaxation multiferroic ceramics which exhibit the highest magnetoelectric coefficient among the known single-phase multiferroic materials[68]. In addition, the coexistence of

polar and magnetic clusters may lead to an ideal stress-strain mediated 'interface' coupling, resulting in large ME effect[69,70]. Although this discussion remains qualitative, it would help stimulate further materials research and theoretical modeling to unveil the microscopic mechanisms of the ferromagnetic ordering and possible magnetoelectric interrelations in this interesting magnetically ordered relaxor ferroelectric solid solution of PFN-BFO.

References

1 N.A. Spaldin & R. Ramesh, *Nat. Mater.*, 2019, **18**, 203-212.

2 C-W. Nan & J-M. Liu, *Natl. Sci. Rev.*, 2019, **6**, 620.

3 M. Bibes, *Nat. Mater.*, 2012, **11**, 354-357.

4 Y. Tokura, *Science*, 2006, **312**, 1481-1482.

5 W. Kleemann, P. Borisov, S. Bedanta & V.V. Shvartsman, *IEEE Trans. Ultrason. Ferroel. Freq. Control.*, 2010, **57**, 2228-2232.

6 F. Li, D. Lin, Z. Chen, Z. Cheng, J. Wang, C. Li, Z. Xu, Q. Huang, X. Liao, L.Q. Chen, T.R. Shrout, S. Zhang, *Nat. Mater.*, 2018, **17**, 349-354.

7 F. Li, M.J. Cabral, B. Xu, Z. Cheng, E.C. Dickey, J.M. LeBeau, J. Wang, J. Luo, S.

Taylor, W. Hackenberger, L. Bellaiche, Z. Xu, L.-Q. Chen, T.R. Shrout, S. Zhang, *Science*, 2019, **364**, 264-268.

8 F. Li, S. Zhang, T. Yang, Z. Xu, N. Zhang, G. Liu, J. Wang, Z. Cheng, Z.-G. Ye, J. Luo, T.R. Shrout & L.-Q. Chen, *Nat. Commun.*, 2016, **7**, 13807.

9 L. Chen, A.A. Bokov, W.M. Zhu, H. Wu, J. Zhuang, N. Zhang, H.N. Tailor, W. Ren and Z.-G. Ye, *Sci. Rep.*, 2016, **6**, 22327.

10 H. Ursic, A. Bencan, U. Prah, M. Dragomir and B. Malic, *Materials*, 2019, **12**, 1327.

11 U. Prah, T. Rojac, M. Wencka, M. Dragomir, A. Bradesko, A. Bencan, R. Sherbondy, G. Brennecka, Z. Kutnjak, B. Malic and H. Ursic, *J. Eur. Ceram. Soc.*, 2019, **39**, 4122-4130.

12 H. Sim, D.C. Peets, Sanghyun Lee, Seongsu Lee, T. Kamiyama, K. Ikeda, T. Otomo, S.-W. Cheong, and J.-G. Park, *Phys. Rev. B*, 2014, **90**, 214438.

13 R. Mackeviciute, V. Goian, S. Greicius, R. Grigalaitis, D. Nuzhnyy, J. Holc, J. Banys, and S. Kamba, *J. Appl. Phys.*, 2015, **117**, 084101.

14 G.L. Platonov, L.A. Drobyshev, Y.Y. Tomashpolskii, Y.N. Venevtsev, *Sov. Phys. Cryst.*, 1970, **14**, 692-695.

15 V. Bonny, M. Bonin, P. Sciau, K.J. Schenk, G. Chapuis, *Solid State Commun.*, 1997, **102**(5), 347-352.

16 S.P. Singh, S. Yusuf, S. Yoon, S. Baik, N. Shin, D. Pandey, *Acta Mater.*, 2010, **58**(16), 5381-5392.

17 S.P. Singh, D. Pandey, S. Yoon, S. Baik, and N. Shin, *Appl. Phys. Lett.*, 2007, **90**, 242915.

18 S.A. Ivanov, R. Tellgren, H. Rundlof, N. W. Thomas, and S. Ananta, *J. Phys: Condens. Mat.*, 2000, **12**, 2393.

19 A. Levstik, C. Filipic, J. Holc, *J. Appl. Phys.*, 2008, **103**(6), 066106.

20 T. Watanabe, K. Kohn, *Phase Transitions*, 1989, **15**(1), 57-68.

21 D. varshney, R.N.P choudhary, C. rinaldi, R.S. katiyar, *Appl. Phys. A*, 2007, **89**, 793-798.

22 R. Font, O. Raymond-Herrera, L. Mestres, J. Portelles, J. Fuentes and J.M. Siqueiros, *J. Mater. Sci.*, 2016, **51**, 6319-6330.

23 A. Mesquita, B.M. Fraygola, V.R. Mastelaro, and J.A. Eiras, *Appl. Phys. Lett.*, 2012, **100**, 172907.

24 I.-K. Jeong, J.S. Ahn, B.G. Kim, S. Yoon, S.P. Singh, and D. Pandey, *Phys. Rev. B*, 2011, **83**(6), 064108.

25 R. Kolesova and M. Kupriyanov, *Phase Transitions*, 1993, **45**(4), 271.

26 Y.X. Wang, W.L. Zhong, C.L. Wang, and P.L. Zhang, *Phys. Lett. A*, 2001, **288**(1), 45-48.

27 S. Matteppanavar, S. Rayaprol, K. Singh, V.R. Reddy, B. Angadi, *J. Mater. Sci.*, 2015, **50**, 4980-4993.

28 S. Matteppanavar, S. Rayaprol, A.V. Anupama, B. Sahoo, B. Angad, *J. Supercond. Nov. Magn.*, 2015, **28**(8), 2465-2472.

29 C. Stock, S.R. Dunsiger, R.A. Mole, X. Li, and H. Luo, *Phys. Rev. B*, 2013, **88**, 094105.

30 R.O. Kuzian, I.V. Kondakova, A.M. Dare, and V.V. Laguta, *Phys. Rev. B*, 2014, **89**, 024402.

31 Y. Yang, J.-M. Liu, H.B. Huang, W.Q. Zou, P. Bao, and Z. G. Liu, *Phys. Rev. B*, 2004, **70**(13), 132101.

32 O. Raymond, R. Font, J. Portelles, and J.M. Siqueiros, *J. Appl. Phys.*, 2011, **109**, 094106.

33 S.T. Dadami, S. Matteppanavar, I. Shivaraja, S. Rayaprol, B. Angadi, B. Sahoo, *J. Magn. Magn. mater.*, 2016, **418**, 122-127.

34 S. Matteppanavar, S. Rayaprol, B. Angadi, B. Sahoo, *J. Alloy Compd.*, 2016, 677, 27-37.

35 I. Grinberga, M.R. Suchomel, P.K. Davies, A.M. Rappe, *J. Appl. Phys.*, 2005, **98**, 094111(1)-094111(10).

36 D. Lebeugle, D. Colson, A. Forget, M. Viret, P. Bonville, J.F. Marucco, S. Fusil, *Phys. Rev. B*, 2007, **76**, 024116(1)-024116(8).

37 D. Lebeugle, D. Colson, A. Forget, M. Viret, *Appl. Phys. Lett.*, 2007, **91**, 022907(1)-022907(3).

38 E.G. González, A. Perejóna, P.E.S. Jiméneza, M.A. Hayward, L.A.P. Maqueda, *J. Eur. Ceram. Soc.*, 2017, **37**, 945-954.

39 J. Wang, J.B. Neaton, H. Zheng, V. Nagarajan, S.B. Ogale, B. Liu, D. Viehland, V. Vaithyanathan, D.G. Schlom, U.V. Waghmare, N.A. Spaldin, K.M. Rabe, M. Wuttig, R. Ramesh, *Science*, 2003, **299**(5613), 1719-1722.

40 J.P. Patel, A. Senyshyn, H. Fuess, D. Pandey, *Phys. Rev. B*, 2013, **88**, 104108 (1)-104108(9).

41 J. Patel, A. Singh, D. Pandey, *J. Appl. Phys.*, 2010, **107**, 104115(1)-104115(7).

42 A. Stoch, J. Maurin, J. Kulawik and P. Stoch, *J. Eur. Ceram. Soc.*, 2017, **37**,1467-1476.

43 S.T. Dadami, S. Matteppanavar, I. Shivaraja, S. Rayaprol, S.K. Deshpande, M.V. Murugendrappa, B. Angadi, *J. Alloy Compd.*, 2017, **724**, 787-798.

44 U. Prah, M. Dragomir, T. Rojac, A. Bencan, R. Broughton, C.-C. Chung, J.L. Jones, R. Sherbondy, G. Brennecka and H. Ursic, *J. Mater. Chem. C*, 2020, **8**, 3452.

45 S.T. Dadami, S. Matteppanavar, I. Shivaraja, S. Rayaprol, S.K. Deshpande, M.V.

Murugendrappa, B. Angadi, Ceram Int., 2017, **43**, 16684-16692.

46 S.T. Dadami, S. Matteppanavar, I. Shivaraja, S. Rayaprol, S.K. Deshpande, and B. Angadi, *AIP. Conf. Proc.*, 2018, **1942**, 140001.

47 S.T. Dadami, S. Rayaprol, S.K. Deshpande, and B. Angadi, *AIP. Conf. Proc.*, 2020, **2220**, 060005.

48 S.T. Zhang, M.H. Lu, D. Wu, Y.F. Chen, and N.B. Ming, *Appl. Phys. Lett.*, 2005, **87**, 262907.

49 Y.P. Wang, L. Zhou, M.F. Zhang, X.Y. Chen, J.-M. Liu, and Z.G. Liu, *Appl. Phys. Lett.*, 2004, **84**(10),1731-1733.

50 S. Matteppanavar, S. Rayaprol, K. Singh, V.R. Reddy and B. Angadi, *J. Mater. Sci.*, 2015, **50**, 4980-4993.

51 W.D. Kingery and M.D. Narasimhan, *J. Appl. Phys.*, 1959, **30**(3), 307-10.

52 R. Stumpe, D. Wagner and D. Bäuerle, *Phys. Status Solidi A.*, 1983, **75**, 143-154.

53 O. Bidault, P. Goux, M. Kchikech, M. Belkaoumi and M. Maglione, *Phys. Rev. B: Condens. Matter.*, 1994, **49**, 7868-7873.

54 D. O'Neill, R.M. Bowman and J.M. Gregg, *Appl. Phys. Lett.*, 2000, **77**, 1520-1522.

55 C.C. Wang and S.X. Dou, *Solid State Commun.*, 2009, **149**, 2017-2020.

56 R.N.P. Choudhary, D.K. Pradhan, C.M. Tirado, G.E. Bonilla and R.S. Katiyar, *J. Appl. Phys.*, 2006, **100**, 084105.

57 J. Kulawik, D. Szwagierczak, *J. Eur. Ceram. Soc.*, 2007, **27**, 2281-2286.

58 W.M. Zhu and Z.-G. Ye, *Ceram Int.*, 2004, **30**, 1435-1442.

59 R. Waser, T. Baiatu, and K.H. Hardlt, *J. Am. Ceram. Soc.*, 1990, **73**, 1654-1662.

60 N. Dhifallah, O. Turki, M.E. Marssi, M. Dammak, H. Khemakhem, *Ceram. Int.*, 2016, **42**, 6657-6663.

61 F.S. Ahmed, K. Taibi, O. Bidault, N. Geoffroy, N. Millot, *J. Alloy Compd.*, 2017,

693, 245-256.

62 A. Rohrbeck, G.D.L. Flor, M.I. Aroyo, M. Gospodinov, U. Bismayer, B. Mihailova, *J. Phys: Condens. Mat.*, 2016, **28**, 475902.

63 E. Palaimiene, J. Macutkevic, J. Banys, A. Kania, *J. Appl. Phys.*, 2014, **116**, 104103.

64 D. Viehland, S.J. Jang, L.E. Cross and M. Wuttig, *J. Appl. Phys.*, 1990, **68**, 2916-2921.

65 A. A. Bokov, Z.-G. Ye, *J. Mater. Sci.*, 2006, **41**, 31-52.

66 M. Arora, P. Chandra Sati, S. Chauhan, M. Kumar, S. Chhoker, *Mater. Lett.*, 2014, **132**, 327-330.

67 W.-M. Zhu, H.-Y. Guo, and Z.-G. Ye, *Phys. Rev. B*, 2008, **78**, 014401.

68 L.F. Henrichs, O. Cespedes, J. Bennett, J. Landers, S. Salamon, C. Heuser, T. Hansen, T. Helbig, O. Gutfleisch, D.C. Lupascu, H. Wende, W. Kleemann, A.J. Bell, *Adv. Fun. Mater.*, 2016, **26**, 2111-2121.

69 M. Soda, M. Matsuura, Y. Wakabayashi, and K. Hirota, *J. Phys. Soc. Japan*, 2011, **80**, 43704-43705.

70 A. Kumar, G. L. Sharma, R. S. Katiyar, R. Pirc, R. Blinc, and J. F. Scott, *J. Phys. Condens. Matter*, 2009, **21**, 382204.

Table of Contents Entry / Graphical Abstract
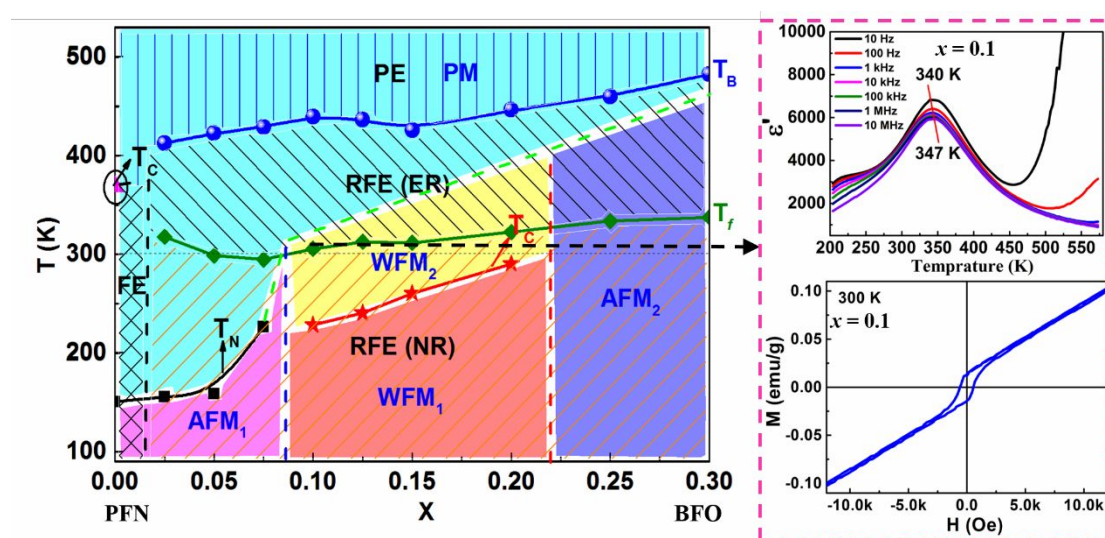
The partial magnetic-ferroelectric phase diagram of the multiferroic $(1-x)Pb(Fe_{1/2}Nb_{1/2})O_3-xBiFeO_3$ ($0 \leq x \leq 0.3$) solid solution system constructed based on the structural, dielectric and magnetic studies. It shows the coexistence of relaxor ferroelectric behaviour and weakly ferromagnetic state at room temperature, making the PFN-BFO system an interesting magnetically ordered relaxor ferroelectric.